Chemical Science

ROYAL SOCIETY OF CHEMISTRY

EDGE ARTICLE

View Article Online
View Journal | View Issue

Cite this: *Chem. Sci.*, 2025, **16**, 16792

All publication charges for this article have been paid for by the Royal Society of Chemistry

Dual-channel deep-NIR-emissive N-embedded PAHs with hybridized local and charge-transfer excited-state

Zuhao Li,[abd] Zhiruo Zhou,[c] Kun Yang,[*de] Yifan Yao,[d] Yaxin Zhai,[c] Dong Wang[*a] and Zebing Zeng[*d]

Polycyclic aromatic hydrocarbon (PAH) molecules have been extensively investigated, and they showcase excellent optoelectronic properties, which are promising for optical applications, including deep-penetration bioimaging and NIR lasers. However, constructing PAHs with deep-NIR (800–1700 nm) photoluminescence is a long-standing challenge, owing to the limitation of the energy gap law. Herein, three N-atom-doped PAHs **APAH-a–c** with electronic acceptor–donor–acceptor (A–D–A) configuration were produced *via* a facile sandwich-like *peri*-fusion pathway. On the basis of these three model molecules, their electronic characters and physicochemical properties were comprehensively studied by X-ray crystallographic analyses, various spectroscopic analyses and theoretical calculations. Our outcomes revealed that core-twisted **APAH-b** and **APAH-c** displayed unique dual-emission with reasonable photoluminescence quantum yield (PLQY) in low-polarity solvents, which were further red-shifted to ~975 nm with increasing solvent-polarity due to their hybridized local and charge-transfer (HLCT) character. In sharp contrast, compound **APAH-a** with a planar π-skeleton did not show any charge-transfer (CT) character or fluorescent solvatochromism effect, indicating a synergistic effect of skeletal nonplanarity and electron-withdrawing N-doping for formation of an HLCT excited-state. Additionally, varying the π-configuration also gives rise to other differentials, such as aromaticity, band gap and open-shell characteristics. In conclusion, our findings offer a valid strategy for the development of deep-NIR-emissive PAH-derivatives *via* fine-tuning the geometrical structure of the π-framework.

Received 10th March 2025
Accepted 5th August 2025

DOI: 10.1039/d5sc01897h

rsc.li/chemical-science

Introduction

Organic near-infrared (NIR)-emitting (700–2500 nm) materials have garnered significant attention due to their unique advantages, including low cost, mechanical flexibility, deep penetration, and biocompatibility, making them highly promising for broad applications, such as high-resolution bioimaging, NIR organic light-emitting diodes (OLEDs), and NIR organic lasers.[1–4] Among these materials, π-conjugated polycyclic aromatic hydrocarbons (PAHs) represent a class of particularly fascinating molecules due to their excellent photostability, high absorbance, tunable band gap, and emissive properties.[5–8] Conventional PAHs typically exhibit fluorescence *via* radiative transitions from a locally excited (LE) state to the ground state (S_0), characterized by a large transition moment with a significant orbital overlap, resulting in a high photoluminescence quantum yield (PLQY) but short emission wavelength within visible regions.[9]

To modulate the light-emitting properties of PAHs, such as the wavelength and PLQY, current approaches primarily involve the enhancement of π-conjugation or the introduction of a charge-transfer (CT) state.[10–12] For example, systematically extending the π-framework facilitates electron delocalization and π-conjugation, giving rise to a narrower band gap accompanied by red-shifted absorption and emission bands.[13–16] However, in view of the energy gap law, a small energy gap (S_0–S_1) could enhance internal conversion and thus block the radiative transition pathway.[17–19] Additionally, extending PAHs always involves tedious chemical syntheses. Conversely, fabricating PAHs with a charge-transfer (CT) character might enable greatly redshifted emission through electron-withdrawing heteroatom-doping like N or B atoms into the π-frameworks (Fig. 1b).[20–24] However, CT-type PAHs generally exhibit low-

[a]*Center for AIE Research, Shenzhen Key Laboratory of Polymer Science and Technology, Guangdong Research Center for Interfacial Engineering of Functional Materials, College of Materials Science and Engineering Shenzhen University Shenzhen, 518060, P. R. China*

[b]*College of Physics and Optoelectronic Engineering, Shenzhen University, Shenzhen 518060, China*

[c]*Key Laboratory of Low-Dimensional Quantum Structures and Quantum Control of Ministry of Education, Department of Physics, Hunan Normal University, Changsha 410081, P. R. China*

[d]*State Key Laboratory of Chemo/Biosensing, and College of Chemistry and Chemical Engineering, Hunan University, Changsha 410082, P. R. China. E-mail: zbzeng@hnu.edu.cn*

[e]*Shenzhen Research Institute, Hunan University, Shenzhen 518000, China*

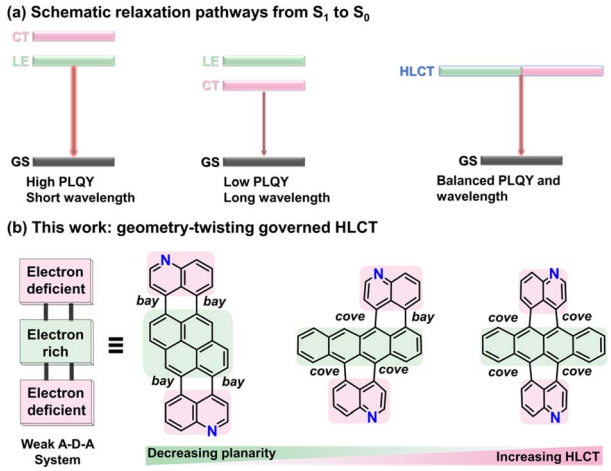

Fig. 1 (a) Illustration of relaxation pathways of a D–A-type π-conjugated system from the excited state (S_1) to the ground state (S_0). (b) Scheme of geometrical twisting-governed HLCT character of **APAH-a–c**.

efficiency photoluminescence, especially in high-polarity environments, due to a decreased transition dipole moment and a slow radiative transition rate.[25–28] Consequently, preparing PAHs with deep-NIR (>800 nm) photoluminescence remains a challenge.

The emerging concept of a hybridized local and charge-transfer (HLCT) state might offer a promising solution. For a quasi-rigid donor–acceptor (D–A) π-conjugated system, an appropriate twisting angle can fine-tune the orbital mixing and the interconverted LE and CT configuration, thereby generating a unique state with admixed LE and CT characters, a so-called HLCT excited-state.[29–31] As a result, the HLCT characteristic guarantees compatibility of the long-wavelength photoluminescence and the large radiative decay rate. Despite the significant potential of HLCT behavior in achieving high-efficiency fluorescence, developing PAHs with intrinsic HLCT behavior remains extremely rare due to the unmanageable equilibrium of the LE and CT states. Until very recently, when Lu *et al.* reported a series of D–A-type heterocycloarenes with a curved π-skeleton, in which one species exhibited a typical HLCT character while the others displayed CT-dominant fluorescence.[32] In this case, these PAHs obviously possess a non-planar π-framework, leading to an appropriate twisting angle between electron-rich and electron-deficient segments upon photoexcitation, which plausibly provides an extra opportunity for the formation of HLCT character. However, the sophisticated mechanism for precise excited-state manipulation of PAHs is as yet ambiguous.

Based on the abovementioned considerations, herein we designed and prepared three doubly N-embedded model molecules, **APAH-a**, **APAH-b** and **APAH-c**, featuring deep-NIR emission tuned by HLCT characters (Fig. 1b). Topologically, the sandwich-like *peri*-fusion of two electron-withdrawing quinoline units (weak acceptor) and one electron-donating tetracene/pyrene (weak donor) moiety might exhibit moderate electronic pull–push interaction and thus prevent an over-expressed CT effect. Conversely, from **APAH-a** to **APAH-c**, increasing *cove*-regions of the π-skeleton give rise to facile variation in molecular geometry upon photoexcitation, which facilitates the disruption of excited-state symmetry and polarized charge separation.[33,34] In this way, the HLCT character could be well controlled by the synergistic effect of electron-withdrawing N-doping and a topologically edged structure. As expected, optical measurements of **APAH-b** and **APAH-c** demonstrated unique polarity-tuned dual emission at the deep-NIR region, attributed to their HLCT characteristic, which was absent for planar **APAH-a**. Additionally, experimental studies accompanied by theoretical calculations unveiled significant differences in their electronic structures and physicochemical properties, such as band gaps and aromaticity. More intriguingly, **APAH-c** showcased a thermally-switched diradicaloid character. Overall, our investigation opens new avenues for exploring excited-state dynamics of aza-PAHs with HLCT characteristics and provides a feasible protocol for developing PAH-based deep-NIR emitters.

Results and discussion

Synthesis and structural characterization

The sophisticated integration of *cove*-edged topologies can impart twisted geometries, increased solubility, and unique π-electronic structures to PAHs.[35–38] However, constructing small-sized PAHs with multiple *cove*-edges, such as the dibenzoterrylene (DBT) molecule, is still a tough challenge because of the robust structural strains.[39–42] Fortunately, the incorporation of a heteroatom into the π-framework might offer an approach for tailoring novel PAHs with greatly twisted π-backbones.[43,44] Herein, *via* a universal two-step synthetic method, three aza-PAHs with either planar (**APAH-a**) or varied degrees of backbone distortion (**APAH-b** and **APAH-c**) were prepared (Scheme 1). Briefly, starting from bis((trimethylsilyl) ethynyl-substituted pyrene/tetracene derivatives that were pre-equipped with solubilizing groups, such as *n*-butyl phenyl or an *n*-butoxy chain, key precursors **1–2** and **2–2** were first prepared *via* a one-pot cascade reaction involving a tandem desiliconization, Povarov [4 + 2] heterocyclization, and oxydehydrogenation with overall yields of 78%/63%.

The resulting brominated quinoline moieties in **1–2**/**2–2** allow **a** further intramolecular cyclodehydrohalogenation process *via* a twofold Heck coupling reaction assisted by a palladium catalyst and a base.[45] Specifically, fully planar **APAH-a** was easily obtained with a satisfying yield of 73% under mild Heck reaction conditions ($Pd(dba)_2$/^{i}PrCOOH/Cs_2CO_3/90 °C). However, likely due to the increased steric hindrance upon the simultaneous formation of multiple spatially crowded *cove*-regions, such conditions failed to afford **APAH-b** and **APAH-c**. Therefore, a systematic screening of reaction conditions (Table S1) was conducted, ultimately revealing that harsher conditions ($Pd(^{t}Bu_3P)_2$/Cs_2CO_3/130 °C) were required to afford the two *cove*-region-containing aza-PAH molecules as a mixture, which was inseparable by conventional purification techniques, such as column chromatography or recrystallization. Considering the possible production of stereoisomers with differential

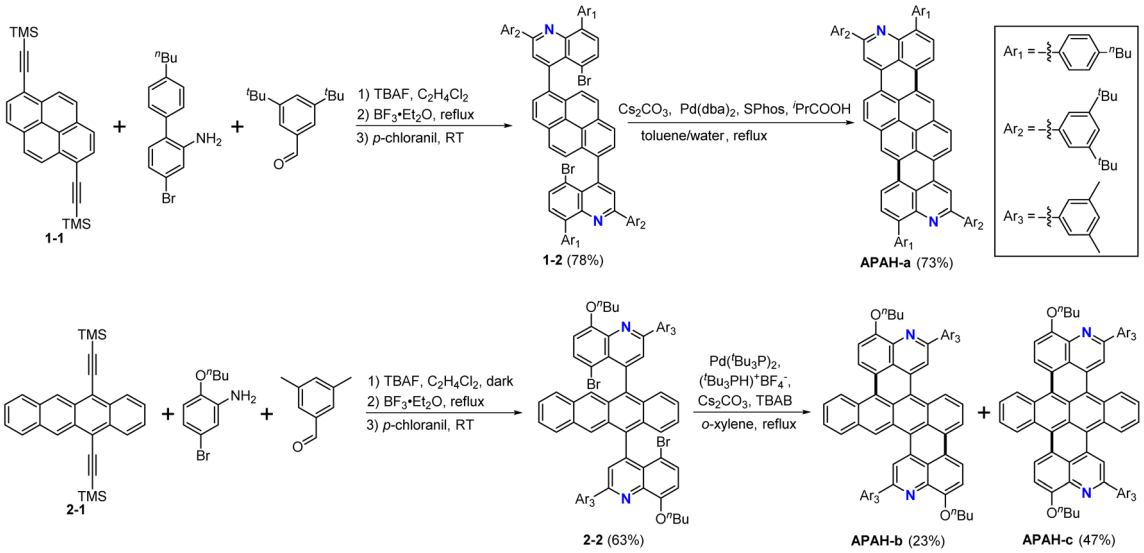

Scheme 1 Synthesis of **APAH-a–c** (TBAF: tetrabutylammonium fluoride; TBAB: tetrabutylammonium bromide; ^{i}PrCOOH: pivalic acid).

geometries, we then chose gel permeation chromatography (GPC) to separate the mixtures to successfully obtain the two stereoisomers with a total yield of 70% (Fig. S1). It is also worth noting that **APAH-b** and **APAH-c** were obtained in an approximate molar ratio of 1 : 2, likely indicating that the C atoms at the inner ring of tetracene have higher reactivity toward the intramolecular cyclodehydrohalogenation process. This separation process indicated that GPC is an effective tool for the isolation of structural isomers, which has rarely been reported in the past.

The resulting aza-PAHs showed moderate solubility in common organic solvents (such as toluene and dichloromethane) and high stability both in the solid state and solution state while stored under ambient conditions. These compounds were also characterized by ^{1}H nuclear magnetic resonance (NMR) spectroscopy and high-resolution mass spectrometry (HRMS), and the results agreed with their corresponding chemical structures. As the ^{13}C NMR spectra of **APAH-b** and **APAH-c** were indistinguishable, 2D ^{1}H–^{1}H NOESY (nuclear Overhauser effect spectroscopy) NMR was further conducted to corroborate their chemical structure (Fig. S2 and S3).

X-ray crystallography

Single crystals suitable for X-ray crystallographic analysis of **APAH-a** and **APHA-b** were successfully obtained by either slow evaporation solution growth or vapor diffusion techniques. However, attempts to grow single crystals of **APAH-c** were unsuccessful. Fortunately, our long-term attempts have led to the serendipitous finding of its dealkylated product (Fig. S4), thereby also providing evidence for the structural accuracy of the **APAH-c** compound. As expected, the resolved single-crystal X-ray structure uncovered an almost planar π-conjugated backbone of **APAH-a** with negligible twisting at its *bay*-regions (Fig. 2a). Despite its bulky benzoic substituents, it was found that two adjacent **APAH-a** molecules are organized into dimeric assemblies with multiple short π–π contacts (3.330–3.354 Å, Fig. S5a), which were further stacked in a tight brickwork packing pattern (Fig. S5b). In sharp contrast, **APAH-b** exhibited a prominently distorted backbone skeleton featuring three *cove* regions and one *bay* area with large dihedral angles of 19.0°–40.2° (Fig. 2b), induced by the substantial steric repulsion between the adjacent hydrogen atoms. As a result, in the crystal lattice, an identical number of stereoisomeric enantiomers were found for **APAH-b** without any close π–π contacts (Fig. S6). Moreover, the DFT-optimized structure of **APAH-c** showed an

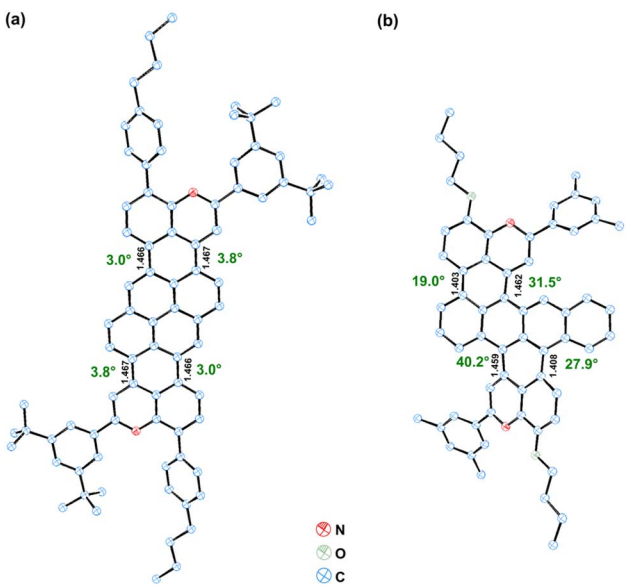

Fig. 2 X-ray crystallographic structures of **APAH-a** (a) and **APAH-b** (b) with highlighted bond-lengths (Å) (black) of the linkage bonds and twisted angles (green) in *bay* and *cove* regions; hydrogen atoms are omitted for clarity.

extremely twisted π-backbone with large dihedral angles of 36.8°–38.7° (Fig. S7). Bond-length analyses revealed that the lengths of linking C–C bonds between two quinoline and the central pyrene units of **APAH-a** were almost equal (1.466–1.467 Å), while those of **APAH-b** displayed very different lengths (*e.g.*, 1.462 *vs.* 1.403 Å), indicating intense strains for the bridged six-membered rings.

Theoretical calculations of aromaticity

Based on their crystallographic structures, the nucleus-independent chemical shift (NICS) values and anisotropy of the induced current–density (ACID) plots of **APAH-a** and **APAH-b** were calculated to probe ring aromaticity upon backbone twisting (Fig. S7 and S8).[46,47] It was revealed that, while the other benzene rings are aromatic, the bridged hexagons of **APAH-a** showed an evident antiaromatic character with positive NICS(1)$_{ZZ}$ values of 12.4 ppm and 12.5 ppm, respectively. For **APAH-b**, however, the NICS(1)$_{ZZ}$ values of the corresponding hexagons were 6.7 ppm and 2.5 ppm, respectively. Such a trend from antiaromatic to nonaromatic character of the two bridged hexagons is in line with the increased ring strains within **APAH-b**. The other hexagons of **APAH-a** and **APAH-b** maintained largely negative values (−11.0 to −23.7 ppm) except for the central ring on **APAH-b**. As depicted in Fig. S7, the ring displayed weak aromaticity (−7.1 ppm) resulting from the bending geometry of the tetracene unit. For **APAH-c**, its DFT-optimized structure was adopted for comparison, which showed that the central rings of its tetracene moiety exhibited weak aromaticity, with NICS(1)$_{ZZ}$ values of −8.8 and −9.4 ppm. The calculated ACID plots further revealed that the planar **APAH-a** exhibited global π-conjugation, as evidenced by a clockwise (diatropic) ring current delocalized along the periphery of the entire π-backbone. In contrast, **APAH-b** showed separately delocalized ring currents over the periphery of both the quinoline and tetracene subunits, likely due to the interference from its backbone twisting. Similarly, **APAH-c** also displayed evident fragmentally delocalized aromaticity for the quinoline and tetracene moieties, as suggested by the ACID plots, agreeing well with its calculated NICD results. Clearly, these results suggest the substantial impact of geometry twisting on the π-electron delocalization pathway of these aza-PAHs.

Optical and electrochemical properties

Fig. 3a depicts the UV-vis-NIR absorption spectra of the three PAHs in their dilute toluene solutions. Compound **APAH-a** displayed a well-resolved absorption band with a maximum (λ_{abs}) at 592 nm (ε = ∼108 000 M^{-1} cm^{-1}, ε: molar extinction coefficient), which can be assigned to the HOMO to LUMO transition on the basis of TD-DFT calculation (Fig. S9 and Table S2). Going on to the two nonplanar aza-PAHs, similar absorption patterns were observed; however, their major absorption bands were significantly red-shifted into the near-infrared regions, with maxima at 772 (ε = ∼98 000 M^{-1} cm^{-1}) and 814 nm (ε = ∼97 000 M^{-1} cm^{-1}) for **APAH-b** and **APAH-c**, respectively, also arising from their HOMO to LUMO transitions (Fig. S10 and S11, Tables S3 and S4). Notably, despite its more twisted molecular geometry, **APAH-c** displayed a 42 nm redshift compared to its regioisomer **APAH-b**, resulting in a narrowed optical energy band-gap (1.25 eV for **APAH-c** *versus* 1.45 eV for **APAH-b**), as estimated from the onset of the lowest energy absorptions. DFT calculations of the frontier molecular orbitals (FMOs) further revealed that the LUMO energy levels of **APAH-a–c** were almost equivalent, whereas the HOMO levels greatly increased from −4.86 eV for **APAH-a** to −4.35 eV for **APAH-b** and −4.29 eV for **APAH-c** (Fig. S12), giving gradually narrowed band gaps and correlating well with the variations in the values obtained from their optical spectra.

The emission behaviors of PAHs were then examined by recording both the steady-state and time-resolved photoluminescence (PL) spectra of **APAH-a–c** in toluene (Table 1). **APAH-a** exhibited intense red fluorescence with emission maximum (λem) at 612 nm (Fig. 3b). Due to its rigid and planar π-framework, the emission profiles of **APAH-a** also resembled its absorption pattern in a mirror-symmetric fashion with a relatively small Stokes shift of 552 cm^{-1}. Compared to **APHA-a**, a broad emission band, covering a broad range of 750–1400 nm, with λ_{em} at 914 nm and a distinct shoulder at ∼845 nm was observed upon excitation at 700 nm for **APAH-b**. Similar to **APAH-b**, the fluorescence spectrum of **APAH-c** displayed a λ_{em} at 915 nm and an obscure shoulder at ∼870 nm upon excitation at 720 nm. The excitation spectra of **APAH-a–c** were measured (Fig. S13), which are coincident with their absorption spectra, proving their intrinsically stimulated radiation behavior. To the best of our knowledge, the fluorescence of **APAH-b** and **APAH-c** accesses the longest wavelength among the previously available N-embedded PAHs, including those with greatly extended π-skeletons (Fig. S16). It is noteworthy that, in comparison with the pristine **DBT** molecule without N-doping, the absorption and emission bands of **APAH-c** exhibit bathochromic-shifts of ∼74 nm and ∼133 nm, respectively, resulting from the enhanced charge-transfer upon electron-withdrawing N-doping.[48]

The absolute photoluminescence quantum yields (PLQYs) of the three aza-PAHs were then determined based on an integrating sphere technique. It was found that **APAH-a** has a PLQY of 74.3% with an excited-state fluorescence lifetime (τ) of 2.86 ns in toluene (Fig. S14), whereas those of **APAH-b** and **APAH-c** in toluene were estimated to be 5.11% and 5.19%, respectively. The depressed PLQYs of **APAH-b/c** compared to **APAH-a** might stem from their combination of flexible π-frameworks and narrowed band-gaps, which cooperatively enhance nonradiative decay channels through vibronic coupling and intramolecular relaxation processes. Intriguingly, the excited-state fluorescence lifetime (τ) of **APAH-b** (τ_1/τ_2 = 0.48/16.20 ns) and **APAH-c** (τ_1/τ_2 = 0.52/16.36 ns) in toluene displayed typically biexponential decay (Fig. S14), implying dual-channel radiative transitions upon photoexcitation, correlating well with their emission profiles, as depicted in Fig. 3b.[49] Such short lifetimes accompanied demonstrations that no triplet excited-state species were formed for either molecule. Moreover, the calculated singlet and triplet energy levels of **APAH-b** and **APAH-c** revealed that both had large S_1–T_1 and S_1–T_2 energy gaps (ΔE_{S1-T1} and ΔE_{S1-}

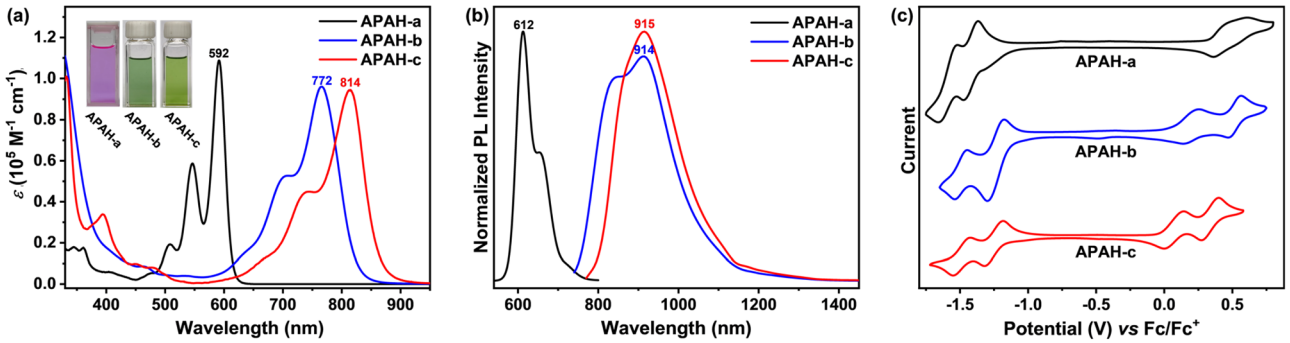

Fig. 3 UV-vis-NIR absorption spectra (a) and normalized photoluminescence spectra (b) of **APAH-a–c** in toluene ($c = 10^{-5}$ M). (c) Cyclic voltammograms of **APAH-a–c** in DCM/$PhCl_2$ with 0.1 M $^nBu_4N^+PF_6^-$ as the supporting electrolyte; the electrode potential was externally referenced to the ferrocene/ferrocenium redox couple.

Table 1 Photophysical properties of **APAH-a–c**

Compounds	λ_{Abs} (nm)	λ_{em} (nm)	ϕ_F (%)	τ (ns)
APAH-a	592	612	74.3	2.86
APAH-b	772	914	5.11	0.48, 16.20
APAH-c	814	915	5.19	0.52, 16.36

$_{T2}$) of 0.39–1.16 eV (Fig. S15), which resulted in ineffective intersystem cross (ISC) pathways. Tentatively, dual radiative transition pathways are plausibly attributed to the hybridization of a local and charge-transfer (HLCT) excited-state (*vide infra*).

The electrochemical characteristics of **APAH-a–c** were investigated by cyclic voltammetry (CV) and differential pulse voltammetry measurements (DPV), showing evident ambipolar redox profiles for the three aza-PAHs (Fig. 3b and S17). Each of them exhibited two reversible reductive curves and two reversible oxidative profiles. More specifically, **APAH-a/b/c** showed first reduction and oxidation potentials of −1.41/−1.24/−1.24 V and 0.33/0.16/0.04 V (*vs.* Fc/Fc^+), respectively. Based on the onset potentials of the first redox transitions, the estimated HOMO energy levels were upshifted from −5.13 eV for **APAH-a**, −4.86 eV for **APAH-b**, to −4.71 eV for **APAH-c**, whereas an identical LUMO energy level of −3.67 eV was found for **APAH-b** and **APHA-c**, both of which were downshifted compared to that of **APHA-a** (−3.49 eV). Accordingly, while an electrochemical band gap of 1.64 eV was calculated for **APAH-a**, the two aza-PAHs, **APAH-b** and **APAH-c**, exhibited profoundly smaller band gaps of 1.19 eV and 1.04 eV, respectively (Table S5). Such narrowed band gaps might give rise to the open-shell electronic characteristics in the PAH-frameworks due to the intensified coulombic repulsions between their valence electrons (*vide infra*).[50,51]

Open-shell characteristics

To verify the abovementioned assumption, spin-unrestricted DFT calculations were performed at (UCAM-B3LYP/6-31G(d,p)) level. These calculations revealed that **APAH-b** and **APAH-c** displayed weak diradical character (y_0 = 6.9% and 9.1%) with large energy gaps between the singlet and triplet states (ΔE_{S-T} = −10.89 and −8.95 kcal mol^{-1}, respectively), thus suggesting a minor contribution from the open-shell resonance structures for those two twisted molecules at room temperature. The diradical character y_0—a dimensionless parameter quantifying the contribution of open-shell resonance configurations to molecular electronic structure (0–100%)—is calculated from the occupation number of the lowest unoccupied natural orbital (LUNO) in spin-projected wavefunction analyses.[52] To validate their open-shell characteristics, variable-temperature ^{1}H NMR and variable-temperature electron spin resonance (ESR) measurements were then carried out. It was found that heating **APAH-b** solution to 373 K led to negligible NMR broadening due to the large ΔE_{S-T} (Fig. S18). Meanwhile, **APAH-b** powder also showed an ESR-silent signal with increasing temperature, confirming that **APAH-b** is more likely to be a fully closed-shell molecule.

In sharp contrast to **APAH-b**, the ^{1}H NMR spectra of **APAH-c** showed a gradual broadening of aromatic resonance signals were observed with the increase in temperature from 273 K to 353 K, likely arising from its thermally excited paramagnetic character (Fig. 4a).[53,54] The resonances of H_c and H_e were found to have almost disappeared at 353 K, which should be attributed to the larger spin populations on their neighboring carbon atoms than the other aromatic protons (Fig. 4c, S19 and S20). For its solid ESR spectra, it was also found that **APAH-c** displayed a negligible ESR signal at room temperature, whereas the intensity increased continuously as the temperature increased from 293 K to 423 K (Fig. 4b), which is a typical characteristic for singlet diradicaloids.[55,56] The g_e factor of **APAH-c** powder was estimated as 2.0028, suggesting that the unpaired spins are ascribed to carbon-based radicals.

To further confirm the thermal-activated open-shell characteristic of **APAH-c**, its variable-temperature absorption spectra were measured in a strictly deaerated tetrachloroethane solution (Fig. S21). As the temperature increased from 293 K to 393 K, the main absorption centered at 815 nm was slightly attenuated, accompanied by an emerging broad band tailing up to 1050 nm. This weak absorbance at the lowest-energy edge can be ascribed to the characteristic forbidden double-excitation

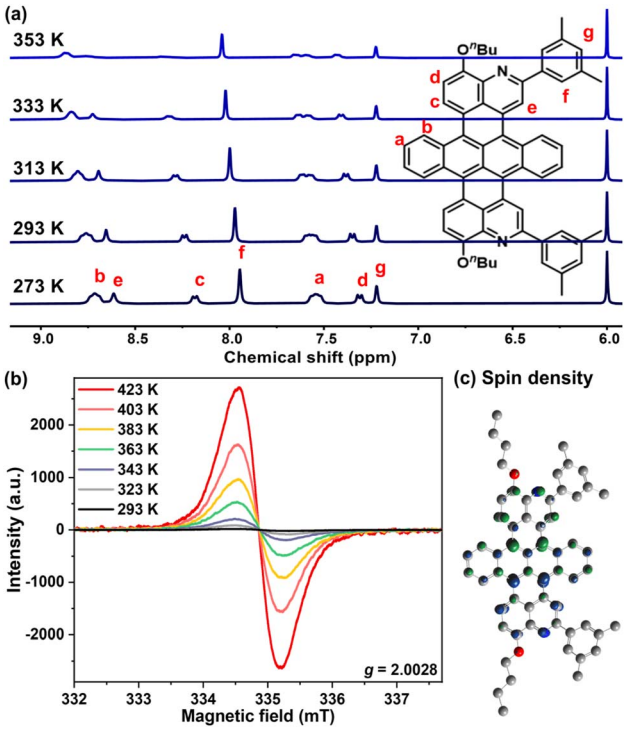

Fig. 4 (a) Variable-temperature ^{1}H NMR spectra (aromatic region) of **APAH-c** recorded in $C_2D_2Cl_4$ (the chemical shift of the solvent molecule is at 6.00 ppm). (b) Variable-temperature ESR spectra of **APAH-c** in solid state. (c) The Mulliken spin density distribution of **APAH-c** (isovalue = 0.008).

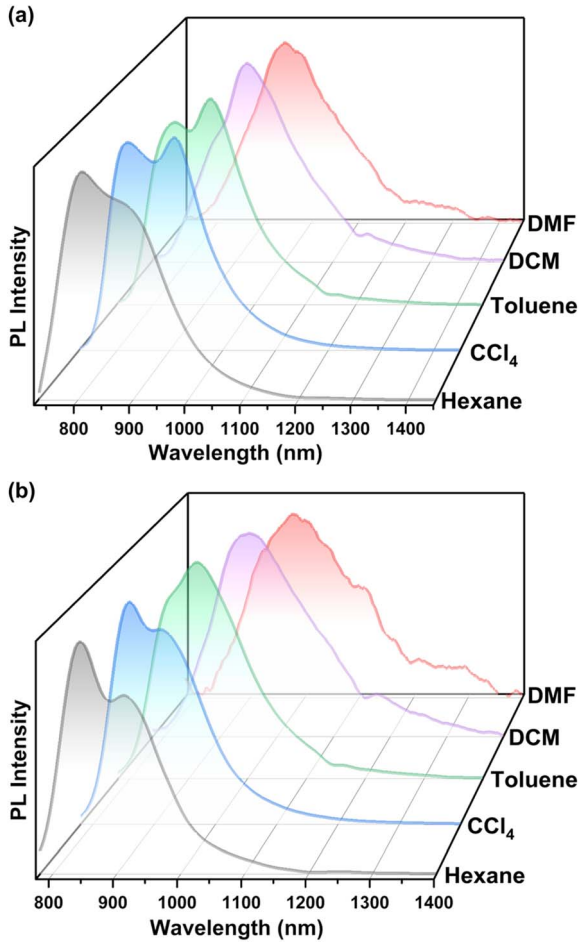

Fig. 5 Photoluminescence profiles of (a) **APAH-b** and (b) **APAH-c** in solvents (1×10^{-5} M) with varying polarities.

state for open-shell diradicaloids.[57] More importantly, such spectral band evolution was found to be totally reestablished with high reversibility after cooling to room temperature. Overall, these results confirm the thermally accessible diradicaloid character of **APAH-c**, which can be as attributed to its greater number of *cove*-regions, leading to robust steric repulsion and intensified coulombic repulsions between their valence electrons compared to the **APAH-b** molecule (which could be relieved by adopting the open-shell form).[51,58]

Photoexcitation dynamics

To shine light onto the possible CT state of these aza-PAHs, their absorption and emission spectra in different solvents with varied polarities were carefully measured. The shapes and positions of the absorption and emission profiles for **APAH-a** were almost maintained in all solvents despite their distinct polarities (Fig. S22 and Table S6). For **APAH-b** and **APAH-c**, however, while their absorption spectra also showed negligible variations as the polarity increased (Fig. S23), obvious variations in emission bands were clearly observed for both molecules (Fig. 5). For instance, in lowest-polar hexane, **APAH-b** exhibited a broad emission band with a maximum at 810 nm and a shoulder at ~898 nm (Fig. 5a). Moving on to tetrachloromethane (CCl_4) with higher polarity, a well-resolved dual-emission band with two peaks at 820 nm and 910 nm was clearly observed. However, with a further increase in solvent polarity, the dual-emission character gradually disappeared, accompanied by a redshift of the emission band with a λ_{em} from 910 nm in CCl_4 to 935 nm in DMF. It was also found that the increase in solvent polarity also caused a gradual decrease in PLQYs from 9.63% in hexane to 0.31% in DMF, as well as significantly enlarged Stokes shifts (from 777 cm^{-1} in hexane to 2342 cm^{-1} in DMF) (Table S7). Such evolutions in emission, including the positive solvatochromism phenomenon (from 845 nm in hexane to 975 nm in DMF), decreased PLYQ (from 14.32% in hexane to 0.23% in DMF), and boosted Stokes shifts (from 496 cm^{-1} in hexane to 2028 cm^{-1} in DMF), were also found for **APAH-c**, revealing the similar impact of backbone twisting on their photophysical properties (Table S8). Moreover, double-exponential analysis of the excited-state decay kinetics for **APAH-b** and **APAH-c** revealed that the fluorescence lifetime components τ_1 and τ_2 exhibit pronounced and contrasting trends with increasing solvent polarity (Fig. S24, Tables S9 and S10). Specifically, the fraction of the shorter-lived component (τ_1) decreases significantly, while that of the longer-lived component (τ_2) increases concomitantly. This evolution in decay kinetics aligns closely with the observed changes in their steady-state emission spectra, providing further compelling

evidence for the polarity-dependent dual excited-state characteristics of **APAH-b** and **APAH-c**.

Given their intriguing variations in emission profiles in different solvents, the excited-state evolutions of **APAH-b** and **APAH-c** were then revealed by classical Lippert–Mataga solvatochromic models.[26] For this purpose, the absorption and emission bands of **APAH-b** and **APAH-c** were measured in various solvents with different orientation polarizability (*f*), and the corresponding Stokes shifts were estimated (Fig. S25–S27; Tables S10 and S11). The Lippert profiles of **APAH-b** and **APAH-c** displayed a typical two-section linear relation, which is characteristic of the HLCT excited-state.[30] Upon transitioning from low-polarity solvents to medium-to-high-polarity media, both compounds exhibited a marked discontinuity in the slope of their Stokes shift–polarity correlation plots. The non-monotonic Stokes shift dependence on solvent polarity, coupled with their pronounced fluorescent solvatochromism, suggests the emergence of polarity-dependent excited-state characteristics—demonstrating progressive evolution from an LE-dominated HLCT state to a CT-dominated configuration as solvent polarity increases.

Moreover, natural transition orbital (NTO) analyses revealed that the hole and electron species of the S_1 state for **APAH-a** were distributed over the whole molecule, while the hole and electron distributions of **APAH-b** and **APAH-c** exhibited partial spatial separation, especially on the tetracene subunit, revealing LE-dominant HLCT characteristics, as mentioned above (Fig. S28).[59–61] Notably, **APAH-b** and **APAH-c**, featuring a multi-*cove* architecture and conformational flexibility in their π-conjugated backbones, undergo substantial dihedral angle reorganizations between the ground state (S_0) and excited state (S_1) (Fig. S29). This structural feature correlates with their unique excited-state dynamics, similar to DBT, underscoring the critical role of molecular topology in modulating photophysical pathways.[48]

To further confirm the existence of HLCT states of **APAH-b** and **APAH-c**, the excited-state relaxation dynamics were investigated using femtosecond transient absorption (TA) spectroscopy. Following a 400 nm laser pulse with 50 fs duration, the time-resolved TA spectra of **APAH-b** and **APAH-c** in CCl_4 and DCM, respectively, were recorded, spanning a wavelength range from 750 nm to 1500 nm (Fig. 6a and b; S30). As shown in Fig. 6a, the spectra in the low-polarity solvent CCl_4 display two broad photo-induced absorption (PIA) features centered at 1152 nm and 1340 nm, which are attributed to the charge-transfer (CT) state and the locally excited (LE) state, respectively. The strong and long-lived ground-state photobleaching (PB) peak at 830 nm correlates with the intense photoluminescence (PL) and high PLQY observed for **APAH-c** in CCl_4. Interestingly, as shown in Fig. 6c, the two PIAs and the PB share the same decay dynamics over a timescale of up to 5000 ps. This behavior reflects the slow vibrational relaxation between the LE and CT states, which facilitates the equilibrium between the two states due to an energy barrier separating them. These findings highlight the role of the solvent in stabilizing the LE and CT states, enabling radiative transitions and extending the excited-state lifetimes.

In contrast, **APAH-c** in DCM, a high-polarity solvent, exhibits a significantly narrowed absorption feature centered at 1340 nm with much faster decay (Fig. 6b and d). The stronger solvent–

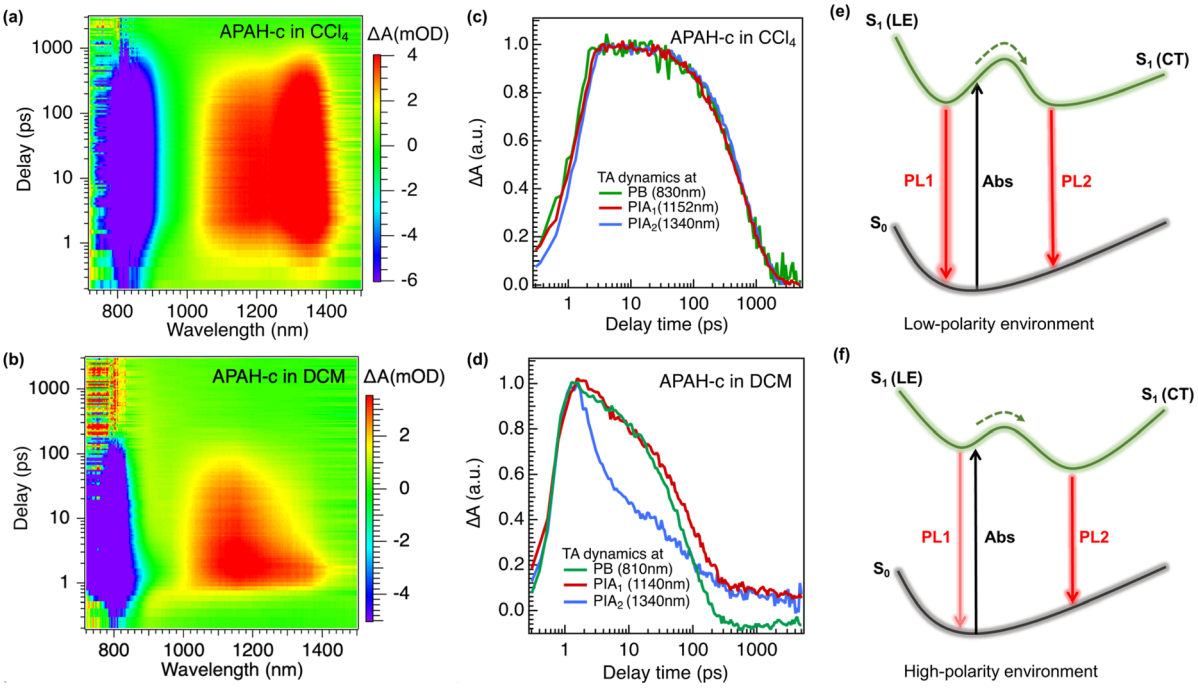

Fig. 6 Pseudo-color representation of fs-TA spectra of **APAH-c** recorded in CCl_4 (a) and DCM (b) following photoexcitation at 400 nm. TA decay dynamics of ground-state photo-bleaching (PB) at 830 nm and photo-induced absorptions (PIAs) for **APAH-c** in CCl_4 (c) and DCM (d). Schematic relaxation pathways in low-polarity (e) and high-polarity (f) solvents after excitation.

solute polarization effect in DCM stabilizes the CT state, lowering its energy level relative to the LE state and favoring its population. The dominance of the CT state results in faster relaxation dynamics, as evidenced by the rapid decay of the photo-induced absorption (PIA) at 1340 nm, with lifetimes of approximately 10 ps. Furthermore, the weaker and faster-decaying PB signal at 810 nm in DCM contrasts with the stronger PB signal in CCl_4, supporting the conclusion that non-radiative decay pathways dominate in high-polarity environments. The narrower energy gap between the CT and ground states in DCM facilitates non-radiative deactivation processes, such as internal conversion (IC), explaining the significantly lower PLQY of **APAH-c** in DCM. Similar measurements were conducted for **APAH-b** (Fig. S30), and the results were consistent with those observed for **APAH-c**.

Based on systematic fs-TA measurements, the excited-state relaxation dynamics of **APAH-b** or **APAH-c** in solvents with different polarities are schematically described in Fig. 6e and f. In a low-polarity solvent, vibrational relaxation from the S_1 (LE) state to the S_1 (CT) state is relatively slow due to the energy barrier, and an equilibrium is established between them. Subsequently, the excited species return to the ground state *via* two radiative transition channels (PL_1 and PL_2) from the lowest, resulting in characteristic dual emission. Meanwhile, a stronger solvent–solute polarization effect in a polar environment lowers the energy of the CT state, and therefore, the excited molecules exhibited a greater population of the CT state rather than the LE state.

Conclusions

In summary, we demonstrated an efficient synthetic pathway to the *peri*-fusion of two electron-withdrawing quinoline segments with one electron-donating tetracene (or pyrene) unit, and consequently obtained a new class of aza-PAHs **APAH-a–c**. The electronic properties of these aza-PAHs were governed effectively by the increasingly twisted π-backbones, which were reflected by their band gaps, optical spectra, and redox potentials. Specifically, **APAH-b** and **APAH-c** with narrow band gaps exhibited deep-NIR photoluminescence with a maximum approximating 1000 nm, a feature very scarce for PAH molecules. Meanwhile, the unique HLCT characters of **APAH-b** and **APAH-c** were unveiled by their fluorescence solvatochromism effect and excited-state dynamics, as well as theoretical calculations, which were not observed for **APAH-a** due to its geometrically planar configuration. Our results also suggested that the thermally accessible open-shell characteristics are relevant to the unique topological twisting. Overall, this study has provided guidance for the future structural engineering of deep-NIR-emissive PAHs with polarity-dependent HLCT excited-states.

Author contributions

Z. Z., D. W. and K. Y. conceived the project. Z. L. conducted the synthesis and carried out the physical characterizations and the major of property studies. Y. Z. and Z. Z. performed the femtosecond transient absorption studies. K. Y. and Z. L. participated in writing the manuscript. Z. Z., K. Y., D. W. and Y. Y. discussed the results and commented on the manuscript. All authors have given approval to the final version of the manuscript.

Conflicts of interest

The authors declare that they have no conflict of interest.

Data availability

The data supporting this article have been included in the SI.

All synthetic protocols, spectroscopic data, SI figures and tables, and detailed crystallographic information can be found in the SI. In detail, these include: synthesis and characterization, NMR and HRMS spectra, data of X-ray crystallographic studies, quantum chemical calculations. See DOI: **https://doi.org/10.1039/d5sc01897h**.

Acknowledgements

The authors thank the National Natural Science Foundation of China (52525306 and 22375059), Special Funds for the Construction of the Science and Technology Project of Hunan Province (2024RC1027), Natural Science Foundation of Hunan Province (2024JJ4013), Guangdong Basic and Applied Basic Research Foundation (2025A1515010687), the National Natural Science Foundation of China (52273174), the National Natural Science Foundation of China (52403158) for financial support.

Notes and references

1 M. Xu, X. Li, S. Liu, L. Zhang and W. Xie, *Mater. Chem. Front.*, 2023, **7**, 4744–4767.
2 Y. Xie, W. Liu, W. Deng, H. Wu, W. Wang, Y. Si, X. Zhan, C. Gao, X.-K. Chen, H. Wu, J. Peng and Y. Cao, *Nat. Photonics*, 2022, **16**, 752–761.
3 K.-W. Lee, Y. Wan, Z. Huang, Q. Zhao, S. Li and C.-S. Lee, *Adv. Mater.*, 2024, **36**, 2306492.
4 Y. Yu, H. Xing, D. Liu, M. Zhao, H. H. Y. Sung, I. D. Williams, J. W. Y. Lam, G. Xie, Z. Zhao and B. Z. Tang, *Angew. Chem., Int. Ed.*, 2022, **61**, e202204279.
5 X.-Y. Wang, X. Yao and K. Müllen, *Sci. China:Chem.*, 2019, **62**, 1099–1144.
6 L. Shi, B. Wang and S. Lu, *Matter*, 2023, **6**, 728–760.
7 Y. Zhang, B. Fu, N. Li, J. Lu and J. Cai, *Chem.–Eur. J.*, 2024, **30**, e202402765.
8 P. Liu, Y. Li, M.-X. Wu, H. Kang, X.-L. Zhao, L. Xu, L. Liu, X. Li, J. Fang, Z. Fang, Y. Cheng, H.-B. Yang, H. Yu and X. Shi, *Sci. China:Chem.*, 2025, **68**, 233–240.
9 H. Huang, N. Li, S. Fu, X. Mo, X. Cao, X. Yin and C. Yang, *Advanced Science*, 2023, **10**, 2304204.
10 Y. Xu, Q. Wang, J. Wei, X. Peng, J. Xue, Z. Wang, S.-J. Su and Y. Wang, *Angew. Chem., Int. Ed.*, 2022, **61**, e202204652.
11 Y. Liu, L. Yuan, J. Guo, W. Sun, Y. Wang and C. Dou, *Angew. Chem., Int. Ed.*, 2023, **62**, e202306911.

12 M. Yang, I. S. Park and T. Yasuda, *J. Am. Chem. Soc.*, 2020, **142**, 19468–19472.
13 L. C. Picciolo, H. Murata and Z. H. Kafafi, *Appl. Phys. Lett.*, 2001, **78**, 2378–2380.
14 A. Zampetti, A. Minotto and F. Cacialli, *Adv. Funct. Mater.*, 2019, **29**, 1807623.
15 Z. Zhang, H. Zhu, J. Gu, H. Shi, T. Hirose, L. Jiang, Y. Zhu, D. Zhong and J. Wang, *J. Am. Chem. Soc.*, 2024, **146**, 24681–24688.
16 G.-F. Huo, W.-T. Xu, J. Hu, Y. Han, W. Fan, W. Wang, Z. Sun, H.-B. Yang and J. Wu, *Angew. Chem., Int. Ed.*, 2025, **64**, e202416707.
17 J. V. Caspar and T. J. Meyer, *J. Phys. Chem.*, 1983, **87**, 952–957.
18 J. V. Caspar, E. M. Kober, B. P. Sullivan and T. J. Meyer, *J. Am. Chem. Soc.*, 1982, **104**, 630–632.
19 Y. Zhang, D. Zhang, T. Huang, A. J. Gillett, Y. Liu, D. Hu, L. Cui, Z. Bin, G. Li, J. Wei and L. Duan, *Angew. Chem., Int. Ed.*, 2021, **60**, 20498–20503.
20 A. Hirono, H. Sakai and T. Hasobe, *Chem.–Asian J.*, 2019, **14**, 1754–1762.
21 J. Wagner, P. Zimmermann Crocomo, M. A. Kochman, A. Kubas, P. Data and M. Lindner, *Angew. Chem., Int. Ed.*, 2022, **61**, e202202232.
22 T. Wang, D. An, J. Zhu, X. Zhang, J. Zhang, Y. Gu, X. Lu and Y. Liu, *Org. Lett.*, 2024, **26**, 5010–5015.
23 W. Sun, Y. Yang, X. Tian, L. Yuan, Y. Wang and C. Dou, *Chem.–Eur. J.*, 2023, **29**, e202302459.
24 J. Cao, W. Zhang, Y. Ding, X. Zhang, Y. Zhang, D. Qiao, S. Biao, X. Dong, J. Song, G. Dai, R. Zhao and Q. Wang, *New J. Chem.*, 2024, **48**, 9014–9019.
25 A. Hirono, H. Sakai, S. Kochi, T. Sato and T. Hasobe, *J. Phys. Chem. B*, 2020, **124**, 9921–9930.
26 Z. R. Grabowski, K. Rotkiewicz and W. Rettig, *Chem. Rev.*, 2003, **103**, 3899–4032.
27 M. Van der Auweraer, Z. R. Grabowski and W. Rettig, *J. Phys. Chem.*, 1991, **95**, 2083–2092.
28 J. Fang, D. An, W. Chen, S. Liu, X. Lu and G. Zhou, *J. Org. Chem.*, 2024, **89**, 4523–4529.
29 W. Li, Y. Pan, R. Xiao, Q. Peng, S. Zhang, D. Ma, F. Li, F. Shen, Y. Wang, B. Yang and Y. Ma, *Adv. Funct. Mater.*, 2014, **24**, 1609–1614.
30 H. Song, K. Wang, Z. Kuang, Y. S. Zhao, Q. Guo and A. Xia, *Phys. Chem. Chem. Phys.*, 2019, **21**, 3894–3902.
31 W. Li, D. Liu, F. Shen, D. Ma, Z. Wang, T. Feng, Y. Xu, B. Yang and Y. Ma, *Adv. Funct. Mater.*, 2012, **22**, 2797–2803.
32 J. Zhu, T. Wang, D. An, R. Zhang, Y. Gu, G. Zhou, X. Lu and Y. Liu, *J. Am. Chem. Soc.*, 2024, **146**, 21922–21931.
33 A. Makarewicz, I. Deperasińska, E. Karpiuk, J. Nowacki and B. Kozankiewicz, *Chem. Phys. Lett.*, 2012, **535**, 140–145.
34 B. Bardi, M. Krzeszewski, D. T. Gryko, A. Painelli and F. Terenziani, *Chem.–Eur. J.*, 2019, **25**, 13930–13938.
35 K. Nagarajan, A. R. Mallia, K. Muraleedharan and M. Hariharan, *Chem. Sci.*, 2017, **8**, 1776–1782.
36 Y. Gu, R. Muñoz-Mármol, S. Wu, Y. Han, Y. Ni, M. A. Díaz-García, J. Casado and J. Wu, *Angew. Chem., Int. Ed.*, 2020, **59**, 8113–8117.
37 Y. Gu, V. Vega-Mayoral, S. Garcia-Orrit, D. Schollmeyer, A. Narita, J. Cabanillas-González, Z. Qiu and K. Müllen, *Angew. Chem., Int. Ed.*, 2022, **61**, e202201088.
38 K. Liu, W. Zheng, S. Osella, Z.-L. Qiu, S. Böckmann, W. Niu, L. Meingast, H. Komber, S. Obermann, R. Gillen, M. Bonn, M. R. Hansen, J. Maultzsch, H. I. Wang, J. Ma and X. Feng, *J. Am. Chem. Soc.*, 2024, **146**, 1026–1034.
39 Z. Sun, W. Fan, Y. Han, W. Yuan, Y. Ni, J. Wang, H. Wei, Y. Zhao, Z. Sun and J. Wu, *Chem. Sci.*, 2023, **14**, 7922–7927.
40 X. Liu, Z. Jin, F. Qiu, Y. Guo, Y. Chen, Z. Sun and L. Zhang, *Angew. Chem., Int. Ed.*, 2024, **63**, e202407547.
41 E. Clar and W. Willicks, *Chem. Ber.*, 1955, **88**, 1205–1207.
42 Chaolumen, M. Murata, A. Wakamiya and Y. Murata, *Angew. Chem., Int. Ed.*, 2017, **56**, 5082–5086.
43 Z. Li, Y. Bu, S. Xie, Y. Ni, K. Yang and Z. Zeng, *Chem. Mater.*, 2024, **36**, 3058–3080.
44 A. Borissov, Y. K. Maurya, L. Moshniaha, W.-S. Wong, M. Żyła-Karwowska and M. Stępień, *Chem. Rev.*, 2022, **122**, 565–788.
45 W. Hagui, H. Doucet and J.-F. Soulé, *Chem*, 2019, **5**, 2006–2078.
46 Z. Chen, C. S. Wannere, C. Corminboeuf, R. Puchta and P. v. R. Schleyer, *Chem. Rev.*, 2005, **105**, 3842–3888.
47 D. Geuenich, K. Hess, F. Köhler and R. Herges, *Chem. Rev.*, 2005, **105**, 3758–3772.
48 C. Erker and T. Basché, *J. Am. Chem. Soc.*, 2022, **144**, 14053–14056.
49 W. Zhang, J. Kong, R. Miao, H. Song, Y. Ma, M. Zhou and Y. Fang, *Adv. Funct. Mater.*, 2024, **34**, 2311404.
50 T. Kubo, *Chem. Lett.*, 2015, **44**, 111–122.
51 Y. Morita, S. Suzuki, K. Sato and T. Takui, *Nat. Chem.*, 2011, **3**, 197–204.
52 K. Yamaguchi, *Chem. Phys. Lett.*, 1975, **33**, 330–335.
53 Y. Gu, H. S. Torchon, Y. Zhu, Z. Wei, D. Schollmeyer, M. Wagner, Y. Ni, Z. Wu, H. Wu, Y. Zhou, Z. Qiu, M. A. Petrukhina and K. Müllen, *Angew. Chem., Int. Ed.*, 2023, **62**, e202307750.
54 Z. Zhou, K. Yang, L. He, W. Wang, W. Lai, Y. Yang, Y. Dong, S. Xie, L. Yuan and Z. Zeng, *J. Am. Chem. Soc.*, 2024, **146**, 6763–6772.
55 C. Zong, X. Zhu, Z. Xu, L. Zhang, J. Xu, J. Guo, Q. Xiang, Z. Zeng, W. Hu, J. Wu, R. Li and Z. Sun, *Angew. Chem., Int. Ed.*, 2021, **60**, 16230–16236.
56 L. Yuan, J. Yang, S. Qi, Y. Liu, X. Tian, T. Jia, Y. Wang and C. Dou, *Angew. Chem., Int. Ed.*, 2023, **62**, e202314982.
57 S. Di Motta, F. Negri, D. Fazzi, C. Castiglioni and E. V. Canesi, *J. Phys. Chem. Lett.*, 2010, **1**, 3334–3339.
58 W. Zeng, H. Phan, T. S. Herng, T. Y. Gopalakrishna, N. Aratani, Z. Zeng, H. Yamada, J. Ding and J. Wu, *Chem*, 2017, **2**, 81–92.
59 T. Lu and F. Chen, *J. Comput. Chem.*, 2012, **33**, 580–592.
60 T. Lu, *J. Chem. Phys.*, 2024, **161**, 082503.
61 G. Li, K. Xu, J. Zheng, X. Fang, W. Lou, F. Zhan, C. Deng, Y.-F. Yang, Q. Zhang and Y. She, *J. Am. Chem. Soc.*, 2024, **146**, 1667–1680.